Dissociation of H_2^+ in intense femtosecond laser fields studied by coincidence three-dimensional momentum imaging

P. Q. Wang, A. M. Sayler, K. D. Carnes, J. F. Xia, M. A. Smith, B. D. Esry, and I. Ben-Itzhak
J. R. Macdonald Laboratory, Department of Physics, Kansas State University, Manhattan, Kansas 66506, USA
(Received 1 July 2006; published 13 October 2006)

The dissociation of H_2^+ in an intense laser field has been experimentally studied using femtosecond laser pulses at 790 nm in the intensity range of 10^{13}–10^{15} W/cm^2. Kinematically complete measurements of both the ionic H^+ and neutral H fragments dissociated from a vibrationally excited H_2^+ beam have been achieved by a coincidence three-dimensional momentum imaging system. Angular-resolved kinetic energy release spectra for a series of different intensity ranges have been obtained using the intensity-difference spectrum method, thus disentangling the problem caused by the intensity volume effect. Our results indicate that the dissociation dynamics are drastically different for "long" (135 fs) and "short" (45 fs) laser pulses at similar high laser intensities. Specifically, bond softening is found to be the main feature in long pulses, while above threshold dissociation is dominant in short pulses whose durations are comparable with the vibrational period of the molecule. Bond softening in short pulses appears at low kinetic energy release with a narrow angular distribution. The experimental results are well interpreted by solving the time-dependent Schrödinger equation in the Born-Oppenheimer representation without nuclear rotation.

DOI: 10.1103/PhysRevA.74.043411 PACS number(s): 33.80.Wz, 33.80.Eh, 42.50.Hz

I. INTRODUCTION

As the simplest molecule in nature, the hydrogen molecular ion H_2^+ plays a fundamental role in the theoretical and experimental investigation of the interaction between intense laser fields and molecules. In recent years there have been numerous theoretical explorations of H_2^+ exposed to intense laser fields (e.g., Refs. [1–7]), as well as several excellent reviews (e.g., Refs. [8,9]). Current laser technology produces intense fields which are comparable with the internal Coulomb field of the molecule and activate various interesting phenomena, among which are bond softening [10–12], bond hardening (vibrational trapping)[13], above threshold dissociation [14–16], zero-photon dissociation [17], charge resonance enhanced ionization [18], laser-induced alignment [19–21], and high order harmonic generation [22]. In an intense laser field the original electronic and nuclear motion of the molecule are distorted. Both theoretical and experimental studies have found that the intense-field phenomena are sensitive to the characteristics of the laser pulse, such as the peak intensity, pulse duration, pulse shape, and wavelength [5,23,24].

Experimental investigation of the various intense-field phenomena in H_2^+ is of current interest. However, due to the obvious experimental difficulties involving studies of ion beams, most of the experiments have actually been performed using neutral H_2 as the target (e.g., Refs. [10–12,17,23,25–27]). In these experiments, the H_2 molecule is ionized and then the daughter H_2^+ ion interacts with the light field within the same laser pulse. A few major differences between studies of H_2^+ produced by laser pulses and by an ion source are enumerated as follows. (i) The ionization of H_2 occurs at intensities of about 1×10^{14} W/cm^2 and higher, which prevents the investigation of laser-induced dissociation of H_2^+ at lower intensities. An H_2^+ ion beam target is not subject to this limitation, especially when prepared in excited vibrational levels. (ii) For a long time the initial vibrational population of H_2^+ from the multiphoton ionization of H_2 was unclear, and was assumed to be a Franck-Condon distribution originating from the $v=0$ state of the precursor H_2. Recently, Urbain *et al.* [28] found that an intense ultrashort laser field preferentially populates lower vibrational states than expected for a Franck-Condon transition, which was confirmed by the calculation of Kjeldsen and Madsen [29]. This implies that the vibrational population of the intermediate H_2^+ depends on the properties of the laser pulse. In contrast, the H_2^+ ion-beam target is typically created by electron impact ionization, which can be treated as a vertical transition where the vibrational population approximately follows the Franck-Condon factors (see, e.g., the experiment of Amitay *et al.* [30]). (iii) Photoionization of H_2 populates the H_2^+ vibrational states coherently, while coherence is lost during the long flight time for an H_2^+ ion beam from the ion source to the interaction region (typically a few μs). (iv) In a neutral H_2 target, the rescattering of the ionized electron can be studied, however, it also complicates the interpretation of the experimental results. (v) Experimentally, when a neutral target is used, the ionic fragments and the photoelectrons can be detected. When an ion-beam target is used, the neutral fragments can also be detected. While in this case the measurement of the photoelectrons is possible in principle, it is still an experimental challenge not yet accomplished due to the existence of a large number of photoelectrons from the residual gas. (vi) The density of a neutral target can be many times larger than that of an ionic target, which more easily allows high statistics data to be collected. These significant differences underline the fact that neutral and ion beam targets can test different physics, making them complementary approaches to understanding the dynamics of molecules in intense laser fields.

Previously, there were only a couple of groups that experimentally explored intense laser-molecule interactions using H_2^+ ion beams. Both of these experiments employ intense femtosecond Ti:sapphire laser pulses at 790 nm

to study the processes of laser-induced dissociation ($H_2^+ + nh\nu \rightarrow H^+ + H$) and ionization ($H_2^+ + nh\nu \rightarrow H^+ + H^+ + e$). Williams *et al.* [31–33] produced an H_2^+ beam using a plasma discharge ion source. In their experiment the kinetic energy release (KER) distribution of the H^+ fragment was measured by combining an electrostatic energy analyzer and time-of-flight (TOF) analysis. The KER distribution of the H fragment was measured separately, from the TOF spectrum of H using a laser polarization along the beam direction. Hänsch and co-workers [34–37] used a similar H_2^+ source. In their experiment, either the neutral fragment H or both H^+ and H fragments were projected onto a microchannel plate with a phosphor anode whose 2D image was recorded by a high resolution CCD camera. The initial 3D momentum distribution of the photofragments was reconstructed by an inverse Abel transform of the CCD image, taking advantage of the cylindrical symmetry of the molecular breakup when linearly polarized light is used.

In the above-mentioned experiments, dissociation was clearly separated from ionization in the spectrum of neutral fragments. However, ionization is harder to separate, as the H^+ spectrum measured by Williams *et al.* [31,32] and the accumulated H^+ and H spectrum measured by Pavicic *et al.* [35,36] include a significant contribution from the dissociation channel. A complete distinction between the dissociation and ionization processes is therefore difficult. As Williams' experiment [31,32] showed, the KER spectrum of the proton from the ionization overlaps with that from the dissociation. Although in both experiments one may obtain the abundance of the ionization channel by subtracting the spectrum of H from that of H^+, this method has some drawbacks. First, this is only accurate when there is substantial ionization compared to dissociation in the KER range of interest. Therefore, it cannot be applied near the ionization appearance intensity. Second, since the H fragments to be subtracted have to be measured in a separate experiment, this method demands a high reproducibility of the experimental conditions, which is not easy in such measurements. To solve this problem a coincidence measurement of the fragments from each dissociation or ionization event is required.

In this paper we report the experimental study of laser-induced dissociation of H_2^+ in an intense femtosecond laser field through a coincidence 3D momentum imaging method. In this method, the H^+ and H fragments from each event are detected simultaneously by a time- and position-sensitive detector, which allows the direct retrieval of the initial 3D momenta of both fragments and generates a high-resolution KER and angular resolved spectrum. While previous experiments [34] showed no substantial dependence on laser pulse duration for pulses longer than 135 fs, our results indicate that a "short" pulse (45 fs) produces dramatically different KER and angular spectra compared to that from a "long" pulse (135 fs). Some of the preliminary results have been reported in a former paper [38]. We have also solved the time-dependent Schrödinger equation by expanding on the Born-Oppenheimer electronic states, which helps interpret the observed features of the experimental spectra for both laser pulses. We will describe our theoretical and experimental methods in the next two sections, followed by the detailed experimental results and their comparison with our theoretical calculations.

II. THEORY

Our calculations followed the standard route of solving the time-dependent Schrödinger equation in the Born-Oppenheimer representation. In this section we briefly describe our specific implementation. We will also give a brief discussion of the adiabatic Floquet potentials for this system, which are useful for the interpretation of our experimental results.

A. Time-dependent Schrödinger equation

Two fundamental assumptions underlie our treatment: (i) the nuclei do not have time to rotate during the pulse and (ii) rotation after the pulse is not significant. For the level of agreement we seek here, these assumptions are justified.

The electronic degrees of freedom are expanded on the field-free Born-Oppenheimer states, leaving coupled time-dependent equations in the internuclear distance R (in atomic units):

$$i\frac{\partial}{\partial t}\mathbf{F}(R,t) = \left[-\frac{1}{2\mu}\mathbf{I}\frac{\partial^2}{\partial R^2} + \mathbf{U}(R) + \mathbf{E}(t)\cdot\mathbf{D}(R)\right]\mathbf{F}(R,t). \tag{1}$$

The matrix $\mathbf{I}$ is the unit matrix, $\mathbf{U}(R)$ is the diagonal matrix of Born-Oppenheimer potentials, μ is the nuclear reduced mass, $\mathbf{D}(R)$ is the matrix of electronic dipole matrix elements, and $\mathbf{F}(R,t)$ is the column vector containing the radial wave function in each channel. The laser field $\mathbf{E}(t)$ is assumed to be linearly polarized along the lab frame z axis with magnitude

$$E(t) = E_0 e^{-(t/\tau)^2}\cos(\omega t). \tag{2}$$

The pulse duration τ is related to the FWHM of the intensity envelope by $\tau = \tau_{\mathrm{FWHM}}/\sqrt{4\ln 2}$; E_0 is the amplitude of the electric field [39]; and ω is the carrier frequency. With the orientation of the nuclear axis fixed at an angle θ relative to the laser polarization, the interaction is

$$\mathbf{E}(t)\cdot\mathbf{D}(R) = E(t)[\cos\theta\mathbf{D}_{\parallel}(R) + \sin\theta\mathbf{D}_{\perp}(R)], \tag{3}$$

where $\mathbf{D}(R)$ is evaluated in the molecular-fixed reference frame. The parallel electronic dipole matrix elements are the matrix elements of z, and the perpendicular elements, of the cylindrical radius ρ. Both elements include the appropriate integration over the azimuthal angle.

The potentials and dipole matrix elements were calculated in the body frame of the molecule for all electronic channels up to $n=4$ of the separated atoms for all possible Λ. Here n is the principle quantum number in the separate atom limit, and Λ is the molecular angular momentum projection on the internuclear axis. For H_2^+, these can be calculated essentially exactly within the Born-Oppenheimer approximation. If the molecule is not aligned with the laser polarization, then the component of the electric field perpendicular to the molecular axis couples states with $\Delta\Lambda = \pm 1$. The Coriolis coupling

is neglected since the nuclei are not allowed to rotate.

Equation (1) is solved using the short time propagator

$$\mathbf{F}(R,t+\delta) = e^{-i\mathbf{H}(t+\delta/2)\delta}\mathbf{F}(R,t). \tag{4}$$

The action of the evolution operator is evaluated approximately by first splitting $\mathbf{H}$,

$$\mathbf{H} = \mathbf{H}_0 + \mathbf{E}(t)\cdot\mathbf{D}(R), \tag{5}$$

then using the usual split operator approximation

$$e^{-i\mathbf{H}(t+\delta/2)\delta} \approx e^{-i\mathbf{H}_0(\delta/2)}e^{-iE(t+\delta/2)\mathbf{D}\delta}e^{-i\mathbf{H}_0(\delta/2)}. \tag{6}$$

Each of these exponentials is, in turn, approximated using the Cayley form

$$e^{-i\mathbf{A}\delta} \approx \frac{\mathbf{I}-i\mathbf{A}\delta}{\mathbf{I}+i\mathbf{A}\delta}, \tag{7}$$

and their action evaluated by solving linear equations. The kinetic energy is approximated with finite differences [40].

Solving Eq. (1) directly poses the usual numerical problems due to the continuum components of the wave function. We thus apply the scaling method [41], which means writing

$$R = \alpha(t)\xi \tag{8}$$

and

$$\mathbf{G}(\xi,t) = \sqrt{\alpha(t)}e^{-(i/2)\mu\alpha\dot{\alpha}\xi^2}\mathbf{F}(R,t). \tag{9}$$

The Schrödinger equation is then transformed into

$$i\frac{\partial}{\partial t}\mathbf{G}(\xi,t) = \left[-\frac{1}{2\mu\alpha^2}\mathbf{I}\frac{\partial^2}{\partial\xi^2} + \mathbf{U}(\alpha\xi) + \mathbf{E}(t)\cdot\mathbf{D}(\alpha\xi) + \frac{1}{2}\mathbf{I}\mu\alpha\ddot{\alpha}\xi^2\right]\mathbf{G}(\xi,t), \tag{10}$$

which is solved as described in Eqs. (4)–(7) with the extra effective potential included in $\mathbf{H}_0$. The scaling parameter $\alpha(t)$ is chosen to be

$$\alpha(t) = \begin{cases} 1, & t < t_0, \\ [1+\gamma^4(t-t_0)^4]^{1/4}, & t \geqslant t_0. \end{cases} \tag{11}$$

The linear dependence on time at large times ensures, among other things, that continuum wave packets never hit the edge of the grid in ξ since in the lab frame the edge of the grid lies at $R_{\max} \to \gamma t \xi_{\max}$.

The solution is propagated until the laser pulse has passed and then is analyzed to extract the total dissociation probabilities and kinetic energy distributions of the nuclei. The dissociation probability is obtained by projecting out the bound states, then integrating the remaining probability density over all space. The kinetic energy distribution is obtained by projecting the final time-dependent wave function onto the continuum energy eigenstates. These states are energy normalized so that the total dissociation probability can be obtained by integrating the KER over all energies.

B. Floquet potentials

The theoretical development of the Floquet treatment was recently reviewed in some detail in Ref. [42], and the results applied in another review [9]. We refer the interested reader to those reviews and give only a brief description here.

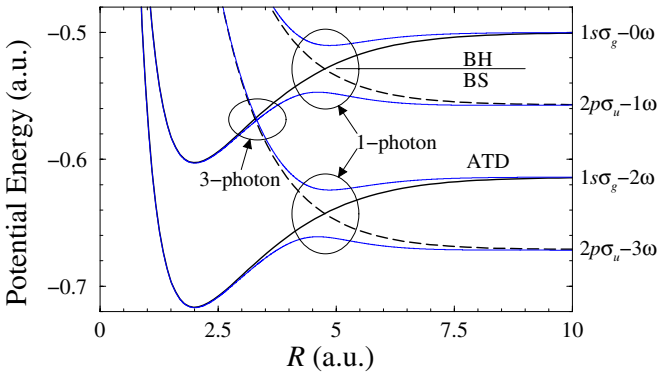

FIG. 1. (Color online) The Floquet potentials for H_2^+. The heavy lines indicate the diabatic Floquet potentials V_{nn}: $1s\sigma_g$ (solid lines) and $2p\sigma_u$ (dashed lines). The adiabatic potentials are shown with light solid lines. The energy ranges for one-photon bond softening (BS) and bond hardening (BH) are indicated.

The key to the utility of the Floquet representation is that it includes the effects of the laser in the Born-Oppenheimer potentials. The Floquet approach, however, does not apply directly to laser pulses. Instead, in its simplest form it assumes a CW laser. So long as the laser pulse has a bandwidth small compared to the carrier frequency (say, roughly 10 or more laser periods within the FWHM of the pulse), the Floquet potentials should provide a reasonable qualitative picture with which the dynamics can be understood. Furthermore, when the pulse satisfies this criterion but is still short compared to the rotational period, the rotation of the molecule can be neglected to a first approximation.

Figure 1 shows the adiabatic Floquet potentials for H_2^+ in a linearly polarized laser with a central wavelength of 790 nm and an intensity of 1×10^{13} W/cm^2. The molecular axis is fixed along the polarization axis. The black lines show the field-free $1s\sigma_g$ and $2p\sigma_u$ Born-Oppenheimer potential curves alternately shifted by the energy of one photon—the diabatic Floquet curves. The blue lines—the adiabatic Floquet curves—show the effect of including the coupling with the laser field: each crossing of the diabatic curves results in an avoided crossing of the adiabatic curves. It is at these crossings that inelastic transitions are most likely to occur.

Before the laser pulse, the H_2^+ molecules are in a distribution of vibrational states in the $1s\sigma_g-0\omega$ curve. As the pulse intensity grows, the diabatic potentials become coupled and the gaps at the avoided crossings get larger at a rate roughly proportional to the electric field strength for crossings between curves coupled by one photon. Vibrational states that lie below the diabatic crossing of the $1s\sigma_g-0\omega$ and $2p\sigma_u-1\omega$ curves now see an effective potential with a barrier. These states can either dissociate over the barrier or by tunneling through the barrier. This process is commonly called bond softening. Vibrational states whose energy is above the crossing also dissociate, but with a lower probability than might be expected. This effective suppression is due to the fact that there is a chance for the nuclei to make an inelastic transition at the avoided crossing to the upper, attractive adiabatic potential. Any flux thus

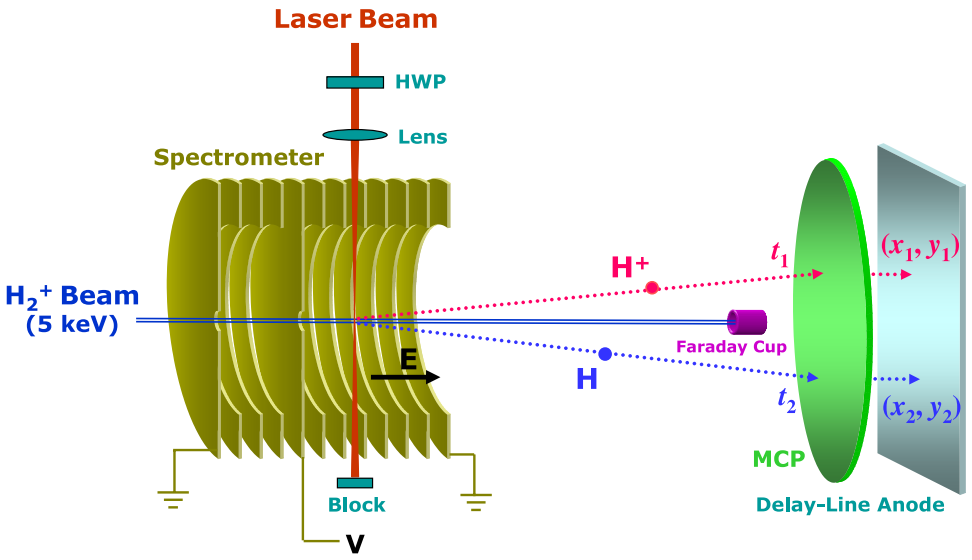

FIG. 2. (Color online) Schematic view of the experimental setup. HWP: half wave plate, MCP: microchannel plate.

trapped does not immediately dissociate, thus reducing the total dissociation probability. This process is commonly labeled bond hardening, or vibrational trapping.

The figure shows calculations for molecules aligned with the field. For molecules at a different angle θ, one simply uses the projection of the field along the molecular axis to calculate the intensity, giving an effective intensity of $I_0 \cos^2 \theta$ where I_0 is the peak intensity at $\theta=0$. This effective intensity is the result of the fact that we are including only the $1s\sigma_g$ and $2p\sigma_u$ electronic states (a good approximation for intensities below roughly 5×10^{13} W/cm^2). As a result, the gaps at the avoided crossings decrease to zero as the angle θ increases from 0° to 90°—a fact that we will use below to understand the angular distributions of the dissociation fragments.

III. EXPERIMENTAL METHOD

Our coincidence 3D momentum imaging method consists of two facets: an experimental setup which allows us to measure the time and position information of each fragment produced in one laser pulse, and a data processing procedure to retrieve the 3D momentum of each breakup event. We have also employed an intensity-difference spectrum method to measure the intensity dependence of the processes under study, which will be discussed at the end of this section.

A. Apparatus

Our experimental setup for studying the interaction between molecular ions and an intense laser field is shown schematically in Fig. 2. The laser pulses are provided by a Ti:sapphire laser system based on chirped-pulse amplification techniques. The output of the laser has a center wavelength of 790 nm, a pulse energy of ~1 mJ, and a repetition rate of 1 kHz. The bandwidth of the laser pulse is ~30 nm, which results in a near Fourier-transform-limited pulse duration of 35 fs (FWHM), measured by a single-pulse autocorrelator. The laser beam is transported to the experimental setup through a vacuum system. The polarization of the laser field is manipulated by a combination of a half-wave plate and a quarter-wave plate. The laser beam is focused by an $f=200$ mm fused silica lens onto the molecular ion beam. The focus of the laser beam has a Gaussian shape in space with a $1/e^2$ diameter of ~65 μm, and a Rayleigh length of ~2.3 mm, measured by a CCD camera. After transmission through all the necessary optics, the laser pulse is broadened to 45 fs at the interaction point. The laser pulse duration is further stretched by introducing a positive chirp, achieved by reducing the distance between the grating pair inside the compressor of the chirped-pulse amplification laser system. The intensity of the laser beam is reduced with beam splitters or neutral density filters.

The H_2^+ beam is produced in an electron cyclotron resonance (ECR) ion source and accelerated to a kinetic energy of 5 keV. The ion beam is collimated to a cross section of ~1×1 mm^2, with a current of ~1 nA. The ion beam is crossed with the laser beam at right angles and is finally directed toward a small Faraday cup (2 mm in diameter) through an electrostatic spectrometer. It is notable that during a period of 100 fs the H_2^+ molecules move only 0.06 μm ahead, which is negligibly smaller than the laser focal size, and thus the ions can be considered as stationary during the interaction. In the present measurement the laser field is linearly polarized along the direction perpendicular to the ion beam, although in principle it can be in any chosen direction. Upon dissociation the two fragments, namely, H^+ and H, acquire a relative momentum and thus spatially separate. In order to clearly distinguish the charged and neutral fragments from each other, a weak longitudinal electric field (typically 20–30 V/mm) is applied along the ion-beam direction to accelerate the ionic fragments in the spectrometer. This results in two distinct peaks in the TOF spectrum, as shown in Fig. 3. The two fragments are detected by a time- and position-sensitive detector, which consists of a microchannel plate of 80 mm diameter and a delay-line anode. The

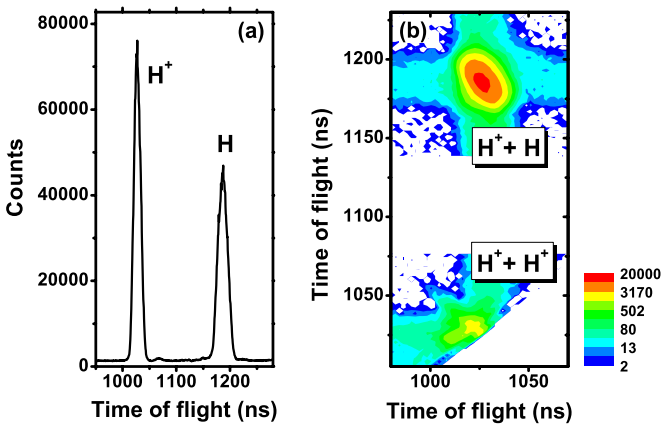

FIG. 3. (Color online) (a) TOF spectrum and (b) coincidence TOF spectrum of H_2^+. Note the TOF separation between the ionic and neutral fragments imposed by the spectrometer field (see text).

distance between the interaction point and the detector is 774 mm. All TOF information is measured relative to the start signal from a photodiode triggered by the laser pulse. The counting rate for true coincidences in laser-induced dissociation is typically 20–40 Hz for the highest laser intensity ($\sim 2\times 10^{15}$ W/cm^2).

B. Data processing

The detector provides both time (from the MCP) and position (from the delay-line anode) signals upon arrival of each fragment, which are recorded event by event, and are used to calculate the 3D momenta of the H^+ and H fragments in the center-of-mass frame. The temporal separation and the coincidence detection of the fragments allow us to directly distinguish the dissociation ($H^+ + H$) and the ionization ($H^+ + H^+$) channels, even though the KER ranges in these two processes partly overlap. As an example, Fig. 3 shows the experimental separation of the H^+ and H fragments in the TOF spectrum, as well as the separation of the dissociation and ionization channels in the coincidence TOF spectrum. The accidental coincidences between H^+ and H (i.e., fragments coming from different molecules), are filtered out by requiring momentum conservation for each dissociation event. This is actually performed by first assuming momentum conservation between any two coincident fragments, then calculating the momentum of the center-of-mass $\mathbf{P}_{\text{c.m.}}$ and finally accepting only the events with $|\mathbf{P}_{\text{c.m.}}| \lesssim 5$ a.u.. The 3D momenta of the fragments provide the angular distributions for the dissociation over the whole 4π solid angle, as well as a high resolution KER spectrum.

The uncertainty of KER is mainly due to the resolution of the detector and time-to-digital converter, which are 0.25 mm in space and 0.5 ns in time, respectively. When the H_2^+ beam energy is 5 keV and the spectrometer voltage is 1 kV, which are typical values for our experiment, the error in the KER is estimated to be $\delta E_{\text{kin}}(\text{eV}) = 0.06 \times \sqrt{E_{\text{kin}}(\text{eV})}$, which is 0.06 eV at a typical KER of 1 eV. The error in $\cos\theta$, where θ is the angle between the laser polarization and the molecular dissociation direction, is estimated to be $\delta\cos\theta = 0.015\sqrt{1+\cos^2\theta/E_{\text{kin}}(\text{eV})}$, which is between 0.015 and 0.021 for $E_{\text{kin}}=1$ eV. It is notable that the uncertainty in both KER and θ can be reduced by improving the spatial and temporal resolutions of the detection system. The coincidence nature of the technique allows us to evaluate the velocity of each molecular ion and measure the fragment velocity in the center-of-mass frame. Compared to previous ion-beam experiments, this kinematically complete measurement eliminates the energy spread as a broadening effect in the momentum resolution.

The performance of the coincidence 3D momentum imaging system can be experimentally tested using the well-studied weak field photodissociation of H_2^+ [43]. In the weak field limit, only the ground state $1s\sigma_g$ and the first excited state $2p\sigma_u$ of H_2^+ are considered. The laser-induced dissociation is a result of a parallel transition between these two states, and thus the yield of the fragments at a given direction is proportional to $\cos^2\theta$. We reduced the laser intensity to about 10^9 W/cm^2 by using an unfocused laser beam and stretching the laser pulse to about 200 fs. The resultant dissociation exhibits the expected $\cos^2\theta$ angular distribution [44].

C. Intensity-difference spectrum

The dynamics of molecules at a certain laser peak intensity is of particular interest. However, most experiments use focused laser beams, where the intensity volume effect caused by the spatial inhomogeneity of the laser intensity is inevitable. The observed spectrum is the sum of the physical phenomena occurring at different intensities ranging from zero up to the peak intensity at the focus, which is referred to as intensity averaging. In order to solve this problem, some special techniques have been used, including theoretical simulations [2] and reducing the dimensions of the target [45]. We recently proposed an intensity-difference spectrum (IDS) method that keeps the exact contribution from a predetermined intensity range and eliminates the contributions from lower intensities. The details of this method have been described elsewhere [46], thus only a brief description is given here. When the size of the molecular beam is much larger than the focal size and much smaller than the Rayleigh range of the laser beam, the actual laser-molecule interaction has a 2D configuration. In this case, when a Gaussian laser beam with a focal radius of w_0 is used, the volume of the target located inside an isointensity shell with a width of dI is $\pi w_0^2 dI/(2I)$, which is independent of the laser peak intensity. The yield of a specific reaction channel measured using a laser pulse with a peak intensity of I_0 is given by

$$S(I_0) = \frac{1}{2}\pi w_0^2 \int_0^{I_0} \frac{P(I)}{I} dI. \tag{12}$$

Here $P(I)$ is the probability for the reaction channel to occur in a laser pulse with peak intensity I. Since the reaction probability is weighted by $1/I$ in this intensity-averaged spectrum, it is possible that the lower intensity ranges have an overwhelmingly higher contribution to the final spectrum. The difference between two experimental results measured at peak intensities I_0 and I_0', where $I_0 > I_0'$, is

$$S(I_0) - S(I_0') = \frac{1}{2}\pi w_0^2 \int_{I_0'}^{I_0} \frac{P(I)}{I} dI. \quad (13)$$

This equation is exactly the contribution from the intensity range between I_0' and I_0, as if we were using a Gaussian beam with a peak intensity of I_0, but spatially truncated at I_0'.

Recall that in our experiment, the width of the ion beam is more than one order of magnitude larger than the laser focus, as experimentally verified by scanning the laser focus across the ion beam, and the thickness is much less than the confocal parameter (twice the Rayleigh length, about 4.6 mm) of the laser beam. Therefore, the IDS method is applicable. We make a sequence of measurements, starting from the maximum available laser intensity, and then gradually attenuating the pulse energy by inserting beam splitters or neutral density filters into the beam path, which reduces the peak intensity while keeping intact the spatial and temporal distribution of the laser beam.

IV. RESULTS AND DISCUSSION

The coincidence 3D momentum imaging method allows us to measure the momenta of both the ionic and neutral fragments, which provides an angular and kinetic energy release spectrum, i.e., a KER-cos θ distribution, for each breakup channel. Here we present our results of the dissociation of H_2^+ using a "long" (135 fs) and "short" (45 fs) laser pulse, and compare them with each other as well as with our theoretical calculations.

A. Long pulses

Figure 4(a) shows the KER-cos θ distribution of laser-induced dissociation of H_2^+ in a laser pulse of 135 fs and a peak intensity of $I_0 = 2.4 \times 10^{14}$ W/cm^2. Here the counts are binned in cos θ since an isotropic spherical distribution will be uniform in that representation. The observed structure matches the $v=7-11$ unperturbed vibrational levels of the ground electronic state. For the vibrational levels below the avoided crossing, the KER may slightly shift to lower values [34], which is an effect accompanying bond softening due to the widening of the potential well formed by the adiabatic potential energy curves. The spectra at a series of lower peak intensities are shown in Figs. 4(b)–4(e). Qualitatively our results are in agreement with that of Sändig *et al.* [34], who also used 135 fs laser pulses. A quantitative comparison between our data and theirs is not possible, because they used a molecular ion beam narrower than the laser focus, which resulted in a quite different intensity averaging.

The observed vibrational structure is more clearly seen in a normal one-dimensional KER distribution. In Fig. 5 we show the KER distribution of Fig. 4(a), but only for the dissociation in the narrow slice of $|\cos\theta| > 0.9$. Compared to Sändig *et al.* [34] we barely see the $v=6$ peak. This is because we have a smaller volume of high intensity in the interaction region. The levels higher than $v=9$ do not appear clearly as the lower levels in this figure. This is because they tend to align away from $|\cos\theta| = 1$, as shown later. For comparison, in Fig. 5 we also show the KER distribution of Fig. 4(c), which is measured at a reduced laser peak intensity. The $v=8$ vibrational level, for example, shifts to lower energy with increasing intensity due to the deformation of the potential well below the avoided crossing.

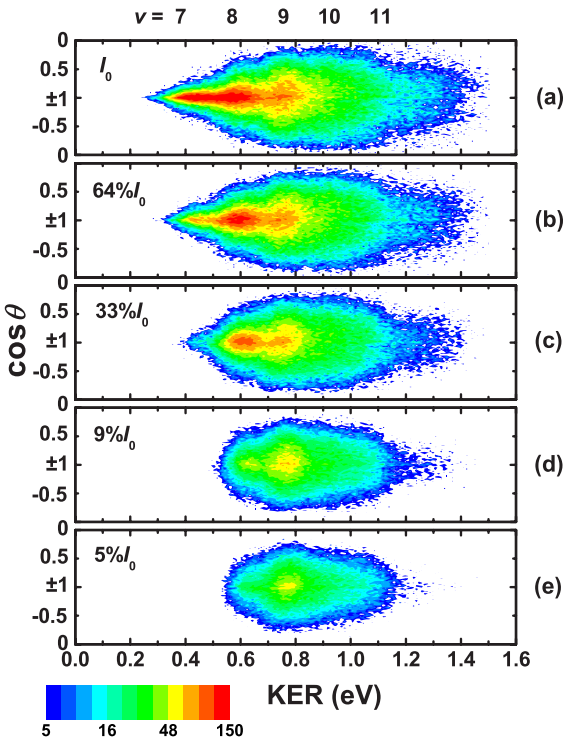

FIG. 4. (Color online) The KER-cos θ distribution of laser-induced dissociation of H_2^+. The pulse duration is 135 fs and $I_0 = 2.4 \times 10^{14}$ W/cm^2. The peak intensities are labeled in each panel. The vibrational structure caused by the levels of the ground electronic state is labeled. Note that cos θ is plotted from 0 to −1, and then from 1 to 0, in order to see the expected symmetry.

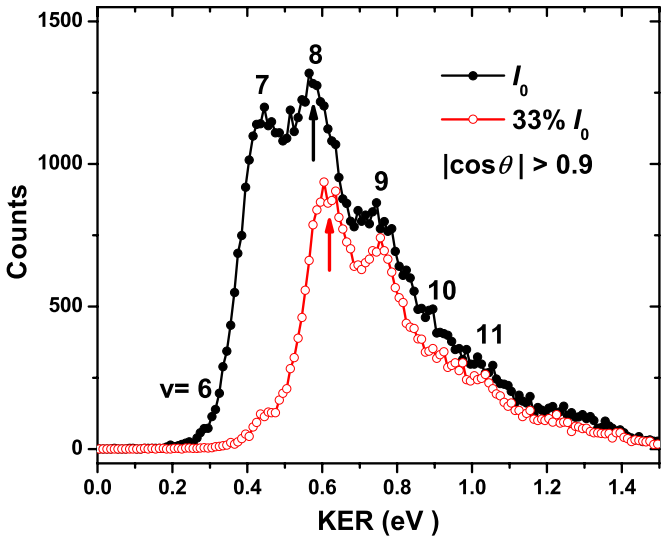

FIG. 5. (Color online) The KER distribution of Fig. 4(a) (filled circles) and Fig. 4(c) (open circles). The arrows mark the KER from the $v=8$ level at each peak intensity. Only the dissociation inside $|\cos\theta| > 0.9$ is taken into account.

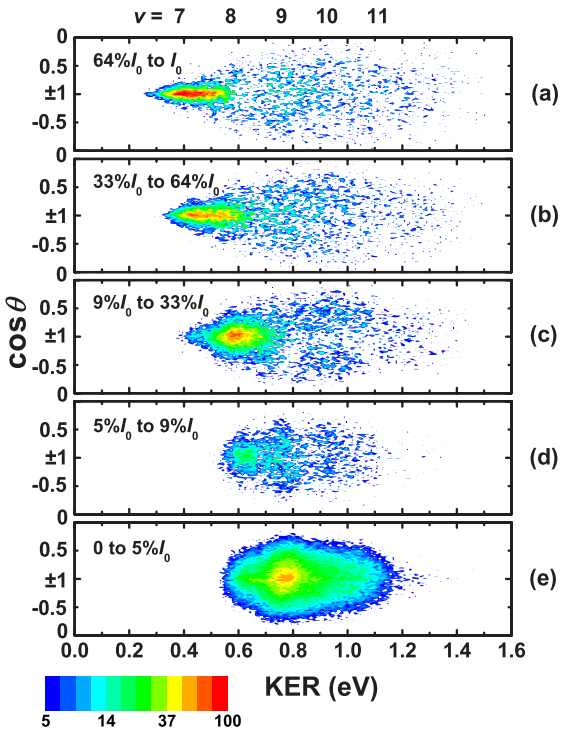

FIG. 6. (Color online) The KER-cos θ intensity-difference spectra of Fig. 4. The corresponding intensity ranges are labeled in each panel.

We now apply the IDS method to the experimental results. By subtracting Fig. 4(b) from Fig. 4(a), Fig. 4(c) from Fig. 4(b), and so on, the spectrum measured at the highest peak intensity, i.e., Fig. 4(a), can be decomposed into five subspectra. Each subspectrum contains the contribution from a certain intensity range. The five components of Fig. 4(a) are shown in Figs. 6(a)–6(e), where Fig. 6(e) is identical to Fig. 4(e) except that the color scale is changed.

The decomposition of the spectrum of Fig. 4(a) by IDS reveals the characteristics of the laser-induced dissociation for specific intensity ranges. For the intensity range below 5% I_0 [Fig. 6(e)], mainly a broad structure around the avoided crossing at about $v=9$ can be seen. This is the typical feature for low-intensity photodissociation. As discussed above, it closely follows a $\cos^2\theta$ distribution as in the weak field limit. It is notable that Fig. 6(e) accounts for 33% of the total counts in Fig. 4(a), although the peak intensity is 20 times smaller. This indicates that an intensity-averaged spectrum may suffer severely from the intensity volume effect, as Eq. (12) implies. In the intensity range of 5–9 $\%I_0$, the broad structure becomes much weaker. Instead, the bond-softening channel from $v=8$ appears stronger, which indicates that the barrier formed by the curve crossing (see Fig. 1) is lower than this vibrational level. At higher intensity ranges, this bond-softening channel is dominant, and it shifts to lower KER in a continuous manner. The shift of the bond-softening channel indicates the successive breakup of lower vibrational levels, as well as a downward energy shift of the levels at higher laser intensities. At the wavelength we used, the dissociation of H_2^+ is dominated by the coupling between the ground ($1s\sigma_g$) and first excited ($2p\sigma_u$) states. The effective light field for this coupling is given by $E_0\cos\theta$, where E_0 is the amplitude of the laser pulse. It is notable that the angular distribution of the bond-softening channel is narrower for the lower vibrational levels. This indicates the strong nonlinear intensity dependence of the avoided crossing energy gap, where the required intensity is only reached when the molecules align within a narrower cone around the laser field direction.

The dissociation from the vibrational levels above the avoided crossing, i.e., $v>9$, forms another feature in Fig. 6. The angular distributions of the dissociation from these levels are much broader than the bond-softening channels, and are even broader than the $\cos^2\theta$ distribution of photodissociation at the weak field limit. Bond hardening can be invoked to explain this broad distribution [47]. Because at higher intensities the molecules can be trapped in the potential well above the avoided crossing, there is a reduced probability for the molecules to dissociate when they align close to the laser polarization, which results in a counterintuitive angular distribution [20]. It is notable that this bond-hardening effect is different from the observation of perpendicular emission of fragments by Talebpour *et al.* [48] at shorter wavelengths, which was interpreted in terms of the coupling between the ground electronic state and the high-lying $3d\sigma_g$ and $3p\pi_u$ states. Although the broadening of the angular distribution of $v>9$ levels can also be caused by saturation, Figs. 4 and 6 indicate that the spectrum for $v>9$ changes when increasing the laser intensity. Therefore the observed phenomenon is attributed to bond hardening rather than saturation.

B. Short pulses

Figure 7(a) shows the KER-cos θ distribution of laser-induced dissociation of H_2^+ in a laser pulse of 45 fs and a peak intensity of $I_0=1.7\times10^{15}$ W/cm^2. The spectra at a series of lower peak intensities are shown in Figs. 7(b)–7(e). The main feature of these spectra is a broad KER distribution around 0.8 eV. After applying the IDS method to the spectra in Fig. 7, we get the spectra for each intensity range as shown in Figs. 8(a)–8(e). The features at lower intensity are generally interpreted by bond softening and bond hardening. However, the IDS spectra indicate that the feature at around 0.8 eV exists at all higher intensities. We propose that this high-intensity feature is produced by above threshold dissociation, where the molecular ion absorbs three photons and emits one later, resulting in a net two-photon absorption. This is confirmed by our calculation, as shown later. From Fig. 8 we also see that at higher intensity ranges, above threshold dissociation generally has a broader KER distribution and shifts slightly to lower KER values.

There is another contribution to the spectra in Fig. 7, which is located below about 0.4 eV, and has a very narrow angular distribution. In the IDS spectra, as shown in Fig. 8, this minor feature shifts to lower KER values when the intensity increases. It becomes weaker at higher intensities, and almost disappears in Fig. 8(a). This suggests that this minor contribution is caused by bond softening, which is confirmed by our calculation as shown later.

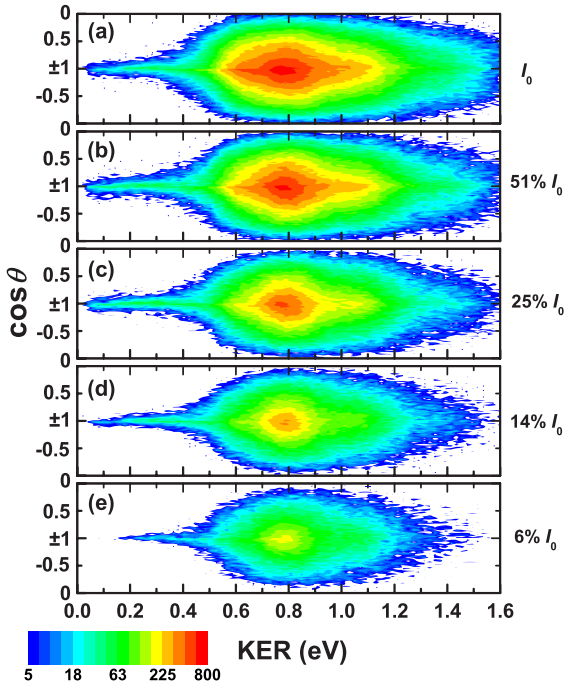

FIG. 7. (Color online) The KER-cos θ distribution of laser-induced dissociation of H_2^+. The pulse duration is 45 fs and $I_0=1.7\times10^{15}$ W/cm^2. The peak intensities are labeled in each panel.

C. Comparison between long and short pulses

It is notable that Fig. 7(d) has almost the same peak intensity as Fig. 4(a), i.e., 2.4×10^{14} W/cm^2, but their spectra

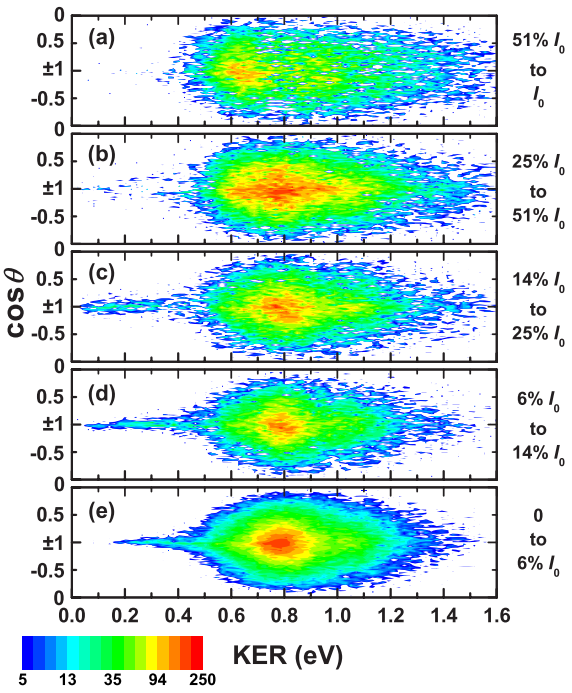

FIG. 8. (Color online) The KER-cos θ intensity-difference spectra of Fig. 6. The corresponding intensity ranges are labeled in each panel.

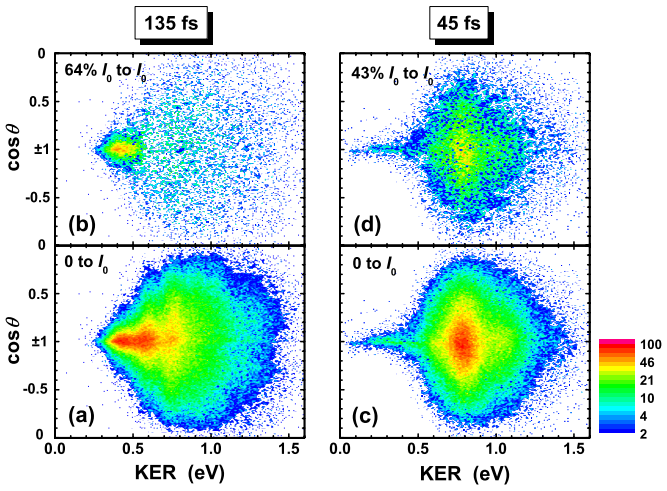

FIG. 9. (Color online) The KER-cos θ distribution of laser-induced dissociation of H_2^+. The peak intensity is $I_0=2.4\times10^{14}$ W/cm^2. (a) The intensity averaged spectrum, for a pulse duration of 135 fs. (b) The IDS spectrum for (a). (c) The intensity averaged spectrum for a pulse duration of 45 fs. (d) The IDS spectrum for (c).

are dramatically different. These two figures and their corresponding IDS spectra are redisplayed in Fig. 9 to show the details. Some significant differences between the spectra of the long and short laser pulses are as follows. (i) At higher intensities, as shown in Figs. 9(b) and 9(d), in the short pulse the dissociation is dominated by above threshold dissociation, while in the long pulse it is mainly due to bond softening and bond hardening. (ii) Vibrational structures can only be observed in the long pulse. They cannot be resolved in the short pulse due to the fact that the 45 fs pulse duration is approaching the vibrational period of H_2^+, which is about 20 fs for the vibration levels from which the molecules dissociate. (iii) The short pulse yields a minor bond-softening channel below 0.4 eV with a narrow angular distribution, which does not appear in the spectrum for the long pulse. The differences between the spectra from the short and the long pulses are more apparent after subtracting the contribution from lower intensities by the IDS method, as shown in Figs. 9(b) and 9(d).

D. Comparison with theory

Before we compare the experimental results with theory, it is helpful to show a typical KER spectrum for H_2^+ dissociation calculated by the method described in Sec. II. Figure 10 shows the total KER distribution for H_2^+ dissociation and contributions from several selected vibrational levels. Here the pulse duration is 45 fs, and the laser intensity is 5×10^{13} W/cm^2. In this figure no intensity averaging is taken into account. For the total KER distribution we calculated the contribution of all levels from $v=0$ to 19. The dissociation mechanisms for $v=9$ and 3 are straightforward. These two levels are located very close to the one-photon and three-photon avoided crossings as shown in Fig. 1. They are subject to bond softening and above threshold dissociation, respectively. However, other vibrational levels may have more

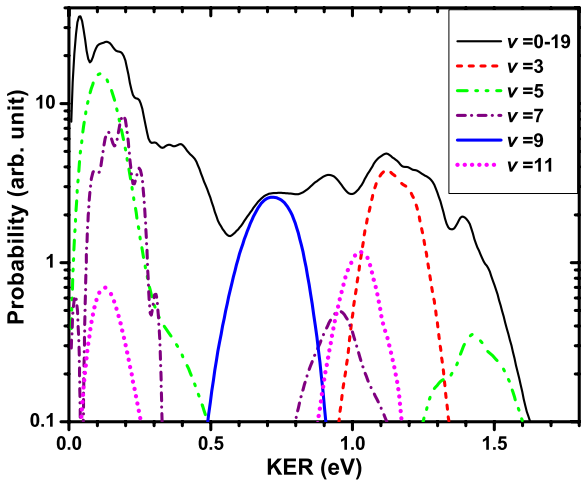

FIG. 10. (Color online) Theoretical KER distribution of laser-induced dissociation of H_2^+. The pulse duration is 45 fs, and the peak intensity is 5×10^{13} W/cm^2. The contributions from several different vibrational levels are shown.

than one dissociation pathway. For example, $v=5$ and 7 can dissociate through both bond softening and above threshold dissociation, where bond softening produces the lower KER peak, and above threshold dissociation produces the higher one. The $v=11$ vibrational level is known to dissociate through bond hardening, but can also produce very low KER at about 0.15 eV. This may be explained by the zero-photon dissociation mechanism suggested by Posthumus *et al.* [17]. In conclusion, Fig. 10 shows that each KER cannot be attributed to one vibrational level, or to one dissociation mechanism. This increases the difficulty of the interpretation of the experimentally observed KER spectrum. Furthermore, in a real experiment the KER distribution is a convolution of spectra at different intensities.

In order to elucidate the experimentally observed phenomena of laser-induced dissociation of H_2^+ at different pulse durations, we calculated the KER-cos θ distribution using the method described in Sec. II. The results are shown in Fig. 11. Here cos θ is obtained using the effective light field along the molecular axis. The peak laser intensity is 1.0×10^{14} W/cm^2, and the pulse duration is 135 fs for Fig. 11(a) and 45 fs for Fig. 11(d). In these two figures no intensity averaging is done. The intensity averaged KER-cos θ distributions are shown in Figs. 11(b) and 11(e). For comparison, the experimental KER-cos θ distributions for 135 and 45 fs laser pulses are shown in Figs. 11(c) and 11(f), which are intensity averaged spectra measured at peak intensities of 1.6×10^{14} and 1.1×10^{14} W/cm^2, respectively.

In our calculation only the ground and first excited electronic states of H_2^+ are considered, and the rotation of the molecule is neglected. On the other hand, the experiments suffer from finite kinetic energy resolution and an uncertainty in the peak intensity ($\sim\pm50\%$). In view of this, we do not expect an exact quantitative agreement between theory and experiment. The theoretical results shown here are intended to guide us in the interpretation of the observed phenomena.

From our calculation shown in Fig. 11(a) we see that in 135 fs laser pulses the dissociation is dominated by one-photon absorption by the molecules initially at different vibrational levels of the ground electronic state. Although it is energetically possible for all $v\geqslant5$ levels to dissociate, the levels around the avoided crossing ($v=9$) contribute the most. At about 1.2 eV a small contribution is superimposed onto the resolved vibrational structure, with a much narrower angular distribution. This minor feature is caused by above threshold dissociation. After intensity averaging, the features at lower intensities, i.e., those at smaller cos θ values in Fig. 11(a) (recall that the effective laser field is given by E_0 cos θ

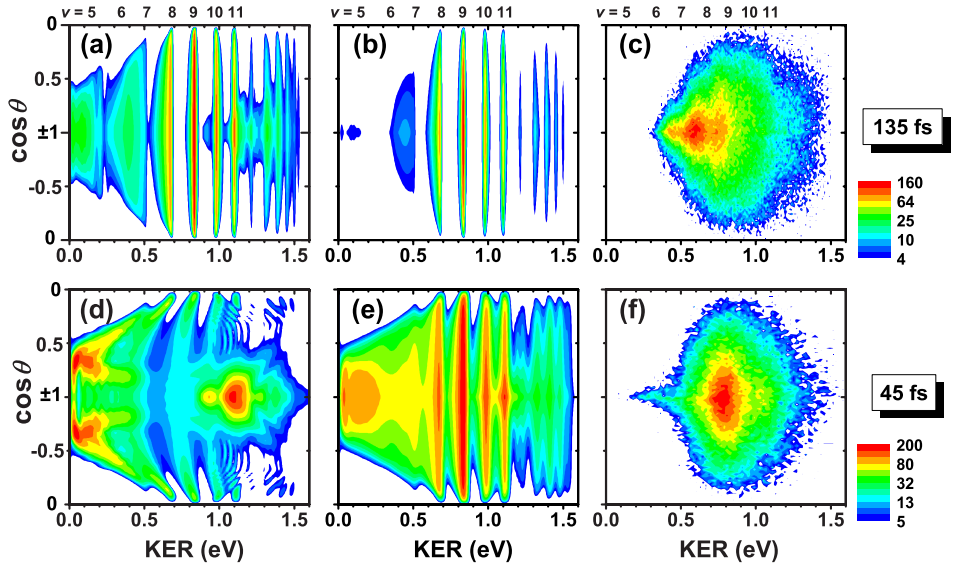

FIG. 11. (Color online) Comparison between experimental and theoretical KER-cos θ distribution of laser-induced dissociation of H_2^+. (a) Theoretical, 135 fs, 1.0×10^{14} W/cm^2, no intensity averaging. (b) Same as (a), but with intensity averaging. (c) Experimental, 135 fs, 1.6×10^{14} W/cm^2. (d) Theoretical, 45 fs, 1.0×10^{14} W/cm^2, no intensity averaging. (e) Same as (d), but with intensity averaging. (f) Experimental, 45 fs, 1.1×10^{14} W/cm^2. The vibrational structure through bond softening and bond hardening are labeled.

and that intensity averaging always enhances the lower-intensity contributions), become dominant in Fig. 11(b). The processes that occur at higher intensities, i.e., the bond softening that produces low KER and the above threshold dissociation at about 1.2 eV, become less apparent. In particular, the dissociation below 0.3 eV, i.e., the bond softening from $v=5$ and 6 levels, seems to be significant in Fig. 11(a), but after intensity averaging it becomes barely noticeable except a spike around 0.1 eV. The bond-softening and bond-hardening channels are reproduced in Fig. 11(c), except that the dissociation below 0.1 eV is not observed. This is because in our experimental setup the fragments with very low KER ($\lesssim$0.1 eV) may not be detected due to the finite size of the Faraday cup used to block the ion beam. It is notable that although above threshold dissociation is a minor channel in 135 fs laser pulses, it has been clearly uncovered in a separate angular distribution analysis [47].

In Fig. 11(d), where 45 fs laser pulses are used, the calculated KER spectrum has two contributions. Below 0.5 eV the bond softening takes place, which peaks at $|\cos\theta| \sim 0.35$. Above 0.5 eV the theoretical spectrum is dominated by another feature with a wide KER range, which is due to above threshold dissociation, where no vibrational structure can be seen. In this KER range bond softening and bond hardening only occur at lower $\cos\theta$ values. After intensity averaging, in Fig. 11(e), the bond-softening and bond-hardening channels are greatly increased, while the above threshold dissociation appears as a background in the KER-$\cos\theta$ distribution. Due to intensity averaging, the bond softening that produces KER below 0.5 eV becomes narrow in angular distribution and now peaks at $|\cos\theta|=1$. These features help us to explain the experimental results as shown in Fig. 11(f). Below 0.5 eV bond softening produces a stripe which is narrow in angular distribution. Above 0.5 eV a large blob is observed in the KER-$\cos\theta$ distribution, which is thought to be a mixture of bond softening and bond hardening at lower intensities, as well as above threshold dissociation at higher intensities. In short laser pulses the vibrational structure in the KER spectrum is broadened, as can be seen by comparing Figs. 11(e) and 11(b). As Fig. 11(f) shows, the vibrational structure in short laser pulses cannot be resolved with our experimental KER resolution.

It is notable that, as Fig. 11 shows, intensity averaging plays an important role in the experiments. Our calculation qualitatively agrees well with the main characteristics of the experimental results. However, a quantitative agreement is still desired.

V. CONCLUSIONS

We have experimentally studied the dissociation of H_2^+ in an intense laser field by a coincidence 3D momentum imaging method. The laser pulses have a wavelength of 790 nm and an intensity range of $10^{13}-10^{15}$ W/cm^2. Our coincidence measurement provides kinematically complete information for the ionic and neutral fragments from each dissociation event and clearly distinguishes the processes of dissociation and ionization. An intensity-difference spectrum method, which takes advantage of the spatial distribution of a Gaussian laser beam, is used to solve the problem caused by intensity averaging. We measured the angular-resolved kinetic energy release spectra at different peak intensities and different pulse durations.

While previous experiments show no significant difference in the spectrum for pulses longer than 135 fs, our results show that the dissociation dynamics are dramatically different for long (135 fs) and short (45 fs) laser pulses at a similar peak intensity. For the long pulse both bond softening and bond hardening appear in the spectrum, and bond softening makes the major contribution. At higher intensities the bond softening dominates in the dissociation, which shifts to lower vibrational levels and has a gradually narrower angular distribution. For the short pulse at higher laser intensities above threshold dissociation is dominant, with a minor contribution from bond softening. A theoretical method for solving the time-dependent Schrödinger equation in the Born-Oppenheimer representation without nuclear rotation is applied, which qualitatively explains our experimental results.

ACKNOWLEDGMENTS

The authors wish to thank Dr. B. Shan and Professor Z. Chang for providing the intense laser beams for this experiment, and Dr. C. Fehrenbach for the ECR beam. This work was supported by the Chemical Sciences, Geosciences and Biosciences Division, Office of Basic Energy Sciences, Office of Science, U.S. Department of Energy.

[1] A. Kondorskiy and H. Nakamura, Phys. Rev. A **66**, 053412 (2002).
[2] V. N. Serov, A. Keller, O. Atabek, and N. Billy, Phys. Rev. A **68**, 053401 (2003).
[3] I. Maruyama, T. Sako, and K. Yamanouchi, J. Phys. B **37**, 3919 (2004).
[4] L.-Y. Peng, I. D. Williams, and J. F. McCann, J. Phys. B **38**, 1727 (2005).
[5] K. C. Kulander, F. H. Mies, and K. J. Schafer, Phys. Rev. A **53**, 2562 (1996).
[6] S. Chelkowski, P. B. Corkum, and A. D. Bandrauk, Phys. Rev. Lett. **82**, 3416 (1999).
[7] B. Feuerstein and U. Thumm, Phys. Rev. A **67**, 043405 (2003).
[8] A. Giusti-Suzor, F. H. Mies, L. F. DiMauro, E. Charron, and B. Yang, J. Phys. B **28**, 309 (1995).
[9] J. H. Posthumus, Rep. Prog. Phys. **67**, 623 (2004).
[10] P. H. Bucksbaum, A. Zavriyev, H. G. Muller, and D. W. Schumacher, Phys. Rev. Lett. **64**, 1883 (1990).
[11] A. Zavriyev, P. H. Bucksbaum, H. G. Muller, and D. W. Schumacher, Phys. Rev. A **42**, 5500 (1990).
[12] A. Zavriyev, P. H. Bucksbaum, J. Squier, and F. Saline, Phys.

Rev. Lett. **70**, 1077 (1993).
[13] L. J. Frasinski, J. H. Posthumus, J. Plumridge, K. Codling, P. F. Taday, and A. J. Langley, Phys. Rev. Lett. **83**, 3625 (1999).
[14] A. Giusti-Suzor, X. He, O. Atabek, and F. H. Mies, Phys. Rev. Lett. **64**, 515 (1990).
[15] T. D. G. Walsh, L. Strach, and S. L. Chin, J. Phys. B **31**, 4853 (1998).
[16] G. Jolicard and O. Atabek, Phys. Rev. A **46**, 5845 (1992).
[17] J. H. Posthumus, J. Plumridge, L. J. Frasinski, K. Codling, E. J. Divall, A. J. Langley, and P. F. Taday, J. Phys. B **33**, L563 (2000).
[18] T. Zuo and A. D. Bandrauk, Phys. Rev. A **52**, R2511 (1995).
[19] J. H. Posthumus, J. Plumridge, L. J. Frasinski, K. Codling, A. J. Langley, and P. F. Taday, J. Phys. B **31**, L985 (1998).
[20] L. J. Frasinski, J. Plumridge, J. H. Posthumus, K. Codling, P. F. Taday, E. J. Divall, and A. J. Langley, Phys. Rev. Lett. **86**, 2541 (2001).
[21] M. Uhlmann, T. Kunert, and R. Schmidt, Phys. Rev. A **72**, 045402 (2005).
[22] T. Zuo, S. Chelkowski, and A. D. Bandrauk, Phys. Rev. A **48**, 3837 (1993).
[23] A. Rudenko, B. Feuerstein, K. Zrost, V. L. B. de Jesus, T. Ergler, C. Dimopoulou, C. D. Schröter, R. Moshammer, and J. Ullrich, J. Phys. B **38**, 487 (2005).
[24] E. E. Aubanel, A. D. Bandrauk, and P. Rancourt, Chem. Phys. Lett. **197**, 419 (1992).
[25] G. N. Gibson, M. Li, C. Guo, and J. Neira, Phys. Rev. Lett. **79**, 2022 (1997).
[26] J. Ludwig, H. Rottke, and W. Sandner, Phys. Rev. A **56**, 2168 (1997).
[27] A. S. Alnaser, X. M. Tong, T. Osipov, S. Voss, C. M. Maharjan, P. Ranitovic, B. Ulrich, B. Shan, Z. Chang, C. D. Lin, and C. L. Cocke, Phys. Rev. Lett. **93**, 183202 (2004).
[28] X. Urbain, B. Fabre, E. M. Staicu-Casagrando, N. de Ruette, V. M. Andrianarijaona, J. Jureta, J. H. Posthumus, A. Saenz, E. Baldit, and C. Cornaggia, Phys. Rev. Lett. **92**, 163004 (2004).
[29] T. K. Kjeldsen and L. B. Madsen, Phys. Rev. Lett. **95**, 073004 (2005).
[30] Z. Amitay, A. Baer, M. Dahan, J. Levin, Z. Vager, D. Zajfman, L. Knoll, M. Lange, D. Schwalm, R. Wester, A. Wolf, I. F. Schneider, and A. Suzor-Weiner, Phys. Rev. A **60**, 3769 (1999).
[31] I. D. Williams, P. McKenna, B. Srigengan, I. M. G. Johnston, W. A. Bryan, J. H. Sanderson, A. El-Zein, T. R. J. Goodworth, W. R. Newell, P. F. Taday, and A. J. Langley, J. Phys. B **33**, 2743 (2000).
[32] W. R. Newell, I. D. Williams, and W. A. Bryan, Eur. Phys. J. D **26**, 99 (2003).
[33] I. D. Williams, B. Srigengan, P. McKenna, W. R. Newell, J. H. Sanderson, W. A. Bryan, A. El-Zein, P. F. Taday, and A. J. Langley, Phys. Scr., T **T 80**, 534 (1999).
[34] K. Sändig, H. Figger, and T. W. Hänsch, Phys. Rev. Lett. **85**, 4876 (2000).
[35] D. Pavičić, A. Kiess, T. W. Hänsch, and H. Figger, Eur. Phys. J. D **26**, 39 (2003).
[36] D. Pavičić, A. Kiess, T. W. Hänsch, and H. Figger, Phys. Rev. Lett. **94**, 163002 (2005).
[37] D. Pavičić, T. W. Hänsch, and H. Figger, Phys. Rev. A **72**, 053413 (2005).
[38] I. Ben-Itzhak, P. Q. Wang, J. F. Xia, A. M. Sayler, M. A. Smith, K. D. Carnes, and B. D. Esry, Phys. Rev. Lett. **95**, 073002 (2005).
[39] We convert between intensity I and atomic units for the electric field using $E_0=5.33799\times10^{-9}\sqrt{I}$ if I is in W/cm^2.
[40] M. W. J. Bromley and B. D. Esry, Phys. Rev. A **69**, 053620 (2004).
[41] E. Y. Sidky and B. D. Esry, Phys. Rev. Lett. **85**, 5086 (2000).
[42] S. I. Chu and D. A. Telnov, Phys. Rep. **390**, 1 (2004).
[43] F. von Busch and G. H. Dunn, Phys. Rev. A **5**, 1726 (1972).
[44] I. Ben-Itzhak, P. Q. Wang, J. F. Xia, A. M. Sayler, M. A. Smith, J. W. Maseberg, K. D. Carnes, and B. D. Esry, Nucl. Instrum. Methods Phys. Res. B **233**, 56 (2005).
[45] P. Hansch and L. D. Van Woerkom, Opt. Lett. **21**, 1286 (1996).
[46] P. Q. Wang, A. M. Sayler, K. D. Carnes, B. D. Esry, and I. Ben-Itzhak, Opt. Lett. **30**, 664 (2005).
[47] P. Q. Wang, A. M. Sayler, K. D. Carnes, J. F. Xia, M. A. Smith, B. D. Esry, and I. Ben-Itzhak, J. Phys. B **38**, L251 (2005).
[48] A. Talebpour, K. Vijayalakshmi, A. D. Bandrauk, T. T. Nguyen-Dang, and S. L. Chin, Phys. Rev. A **62**, 042708 (2000).